6

COUPLED POTENTIALS FOR ELECTROMAGNETIC FIELDS IN INHOMOGENEOUS MEDIA

M. A. Morgan

6.1 Introduction

Electromagnetic interaction with complex inhomogeneous structures has become a topic of expanded interest within the computational fields community in recent years. This has resulted, at least in part, from advances in the incorporation of materials in the engineering design of modern electronics such as antennas, scatterers, lenses, waveguiding and coupling structures, active devices and multilayer high-speed integrated circuits. Even with the processing power of large mainframes there exists limits on the levels of material complexity and physical wavelength dimensions that can be practically accommodated due to computation time and memory constraints.

The analytical and numerical formulations which are employed in the solution of a given field problem play key roles in the requisite computational requirements. This influence is reflected in *both* the number of discrete unknowns generated and in the density of explicit interactions between these unknowns. Classical TE and TM potential formulations, as generalized by Bromwich in 1919 [1], may be used to represent the six vector components of the electromagnetic field using two uncoupled scalar potentials in selected separable coordinate systems. Such TE and TM potential representations are restricted to uniform media and some special cases of one-dimensional inhomogeneity such as spherical stratification.

In the mid-1970's, the use of dual scalar potentials was extended to rotationally symmetric materials, having arbitrary inhomogeneity in the other two dimensions, through the development of the coupled azimuthal potential (CAP) formulation by Morgan, Chang and Mei [2–4]. The CAP representation utilizes two continuous potentials to generate the Fourier azimuthal modes of the time-harmonic vector field. It has since been used as the basis for finite element solutions of radiation, scattering and penetration problems, [5–11].

A two-fold generalization of the CAP formulation is presented here, one which removes both the restriction to axisymmetry of the inhomogeneous media and extends the development to general orthogonal curvilinear coordinates. This new coupled potential (CP) formulation retains two attributes of the original CAP representation: (1) the 6 field unknowns in Maxwell's time-harmonic equations are generated by two scalar potential functions; and (2) partial differential equations are used, resulting in sparse global system matrices. These two properties reduce both the number of discrete unknowns and the density of coupling between the unknowns. The solution of open region radiation and scattering problems can be approached by use of one of the exterior region coupling schemes such as the unimoment method [12], the field feedback formulation [13], or a near-field radiation boundary condition [14].

The analytics of the generalized CP formulation will be presented in the following section, with developments first made in curvilinear orthogonal coordinates and then specifically applied in the circular cylindrical system. The generating equations for the vector fields will initially be considered followed by variational and weighted residual solution approaches for the potentials. Efficient numerical methods for solving these equations will be developed in section 6.3. This will be followed, in section 6.4, by validations of the accuracy and convergence of the resultant algorithms. Included are tests of the vector field generation, using *natural* basis functions, as well as a solution demonstration of the Galerkin equations for a simple 3-D boundary value problem, using a sparse matrix block decomposition technique.

In the final section of this chapter, some future enhancements of the CP formulation and its pending application to scattering by complex material structures will be discussed.

6.2 Coupled Potential Formulation

a. *Fields in Orthogonal Coordinates*

In developing the CP formulation, we will use an impedance normalized phasor magnetic field: $\overline{H} = -j\eta_0 \overline{\mathcal{H}}$, where $\overline{\mathcal{H}}$ is the usual magnetic field, having SI units of A/m, and η_0 is the free-space wave impedance of $120\pi\ \Omega$. The normalized $\overline{H}$ thus has the same V/m units as the usual electric field, $\overline{E}$. A simplified set of Maxwell's source-free curl equations results, being written here using coordinate-free notation,

$$\nabla \times \overline{E}(\overline{r}) = k_0\, \mu_r(\overline{r})\, \overline{H}(\overline{r}) \tag{1a}$$

$$\nabla \times \overline{H}(\overline{r}) = k_0\, \epsilon_r(\overline{r})\, \overline{E}(\overline{r}) \tag{1b}$$

where $k_0 = 2\pi/\lambda_0$ is the wavenumber, while $\epsilon_r(\overline{r})$ and $\mu_r(\overline{r})$ are the relative dielectric and magnetic parameters in the inhomogeneous media. The constitutive parameters, $\epsilon_r(\overline{r})$ and $\mu_r(\overline{r})$, may be either piecewise constant or continuously variable spatial functions. For regions containing lossy material one or both of these functions will be complex.

We will initially develop two versions of the generating equations which provide the vector fields in terms of two scalar coupled potentials. One of these forms will use dual first order partial differential equation (PDE) systems, each having the form of a transport equation. The other development will take the form of second-order PDE systems which will be used later to construct the natural basis functions for the numerical application in circular cylindrical coordinates.

To begin the CP derivation, we will employ a generic right-hand system of curvilinear orthogonal coordinates, to be denoted by (u_1, u_2, u_3) where each u_i is some specified function in the cartesian space (x, y, z). At each spatial point, local unit vectors are defined by

$$\widehat{u}_i = \frac{\nabla u_i}{|\nabla u_i|} \quad \text{for } i = 1,3 \tag{2}$$

The field vectors are then expressible in component form using the unit vector basis at each point. For example,

$$\overline{E}(\overline{r}) = E_1(\overline{r})\,\widehat{u}_1 + E_2(\overline{r})\,\widehat{u}_2 + E_3(\overline{r})\,\widehat{u}_3 \tag{3}$$

The local unit vectors at each point form an *orthonormal* basis, as illustrated in Fig. 1. An additional constraint will be imposed on the coordinate system to be used in the current application, as will be addressed shortly. There will, however, be *no need* for separable coordinates with the differential operators to be employed. As a result, a virtual infinity of custom coordinate systems can be designed for applications of this formulation. Such coordinates may, for instance, be made conformal to the external surface of some complicated metallic object.

We next need to define scale factors, h_i, to transform differential coordinate variations, du_i to the corresponding metrical changes in arc length, $ds_i = h_i\, du_i$ for $i = 1,3$. For example, in the spherical coordinate system, with $(u_1, u_2, u_3) = (r, \theta, \phi)$, we have $h_1 = 1$, $h_2 = r$ and $h_3 = r \sin\theta$. Using subscript notation for partial derivatives, (e.g. $D_1 = \partial/\partial u_1$), the curl equations in (1) become

$$D_2(h_3\, E_3) - D_3(h_2\, E_2) = \mu_r \alpha_1 (h_1\, H_1) \tag{4a}$$

$$D_3(h_1\, E_1) - D_1(h_3\, E_3) = \mu_r \alpha_2 (h_2\, H_2) \tag{4b}$$

$$D_1(h_2\, E_2) - D_2(h_1\, E_1) = \mu_r \alpha_3 (h_3\, H_3) \tag{4c}$$

$$D_2(h_3\, H_3) - D_3(h_2\, H_2) = \epsilon_r \alpha_1 (h_1\, E_1) \tag{4d}$$

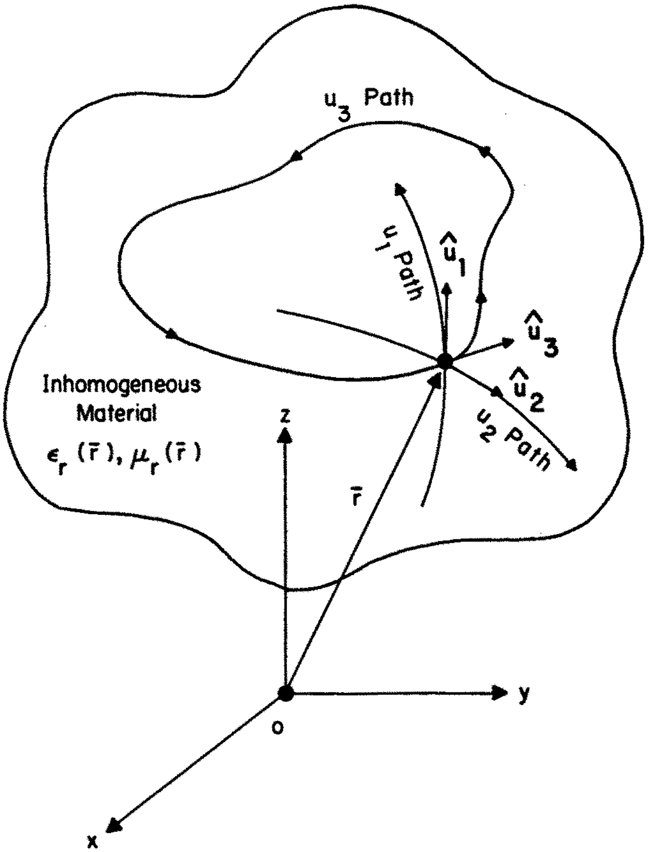

Figure 1 **Orthogonal coordinate contours in inhomogeneous material.**

$$D_3(h_1 H_1) - D_1(h_3 H_3) = \epsilon_r \alpha_2 (h_2 E_2) \tag{4e}$$

$$D_1(h_2 H_2) - D_2(h_1 H_1) = \epsilon_r \alpha_3 (h_3 E_3) \tag{4f}$$

where $\alpha_i(\bar{r})$ are wavenumber normalized scale factor ratios

$$\alpha_1(\bar{r}) = k_0 \frac{h_2 h_3}{h_1} \tag{5a}$$

$$\alpha_2(\bar{r}) = k_0 \frac{h_1 h_3}{h_2} \tag{5b}$$

$$\alpha_3(\bar{r}) = k_0 \frac{h_1 h_2}{h_3} \tag{5c}$$

b. Transverse Field Generation

Using (4a), (4b), (4d) and (4e), we can define CP's in terms of E_3 and H_3 to drive dual systems of first-order differential equations (DE's) for the remaining four vector field components. These coupled systems are written in matrix form as

$$D_3 \overline{V}_p + \overline{\overline{M}}_p \cdot \overline{V}_p = \overline{U}_p \quad \text{for } p = 1,2 \tag{6}$$

The cross-coupling arrays in (6) are given by

$$\overline{\overline{M}}_1(\bar{r}) = \begin{bmatrix} 0 & \mu_r \alpha_2 \\ -\epsilon_r \alpha_1 & 0 \end{bmatrix} \tag{7a}$$

$$\overline{\overline{M}}_2(\bar{r}) = \begin{bmatrix} 0 & \mu_r \alpha_1 \\ -\epsilon_r \alpha_2 & 0 \end{bmatrix} \tag{7b}$$

while the transverse (to $\hat{u}_3$) field arrays are defined by

$$\overline{V}_1(\bar{r}) = \begin{bmatrix} h_1 E_1 \\ -h_2 H_2 \end{bmatrix} \tag{8a}$$

$$\overline{V}_2(\bar{r}) = \begin{bmatrix} h_2 E_2 \\ h_1 H_1 \end{bmatrix} \tag{8b}$$

The CP's, which are defined by

$$\psi_1(\bar{r}) = h_3(\bar{r}) E_3(\bar{r}) \tag{9a}$$

$$\psi_2(\bar{r}) = h_3(\bar{r}) H_3(\bar{r}) \tag{9b}$$

are differentiated to form the driving arrays in (6)

$$\overline{U}_1(\overline{r}) = \begin{bmatrix} D_1 \psi_1 \\ \\ -D_2 \psi_2 \end{bmatrix} \tag{10a}$$

$$\overline{U}_2(\overline{r}) = \begin{bmatrix} D_2 \psi_1 \\ \\ D_1 \psi_2 \end{bmatrix} \tag{10b}$$

The generating equations in (6) may, in principle, be solved for the transverse fields in terms of the CP derivative driving arrays. A unique solution, however, is predicated upon specified boundary conditions (BC's) on the unknown vectors, $\overline{V}_p$. In the computational portion of this work, to be described in section 6.3, cyclic BC's are used with (6). To this end, the $u_3(x, y, z)$ coordinate is assumed to be periodic, thus forming closed contours in space, as is illustrated in Fig. 1. Some example coordinate systems that fit this description are elliptic cylindrical, spheroidal, paraboloidal as well as the more standard circular cylindrical and spherical systems, [15]. Although a cyclic u_3-coordinate is defined in this application, it is conceivable that the CP formulation can be employed without such a restriction.

An alternate, second-order set of generating equations for the non-$\widehat{u}_3$ field components results from a judicious substitution within the first-order systems in (6)

$$\overline{\overline{L}}_e \cdot \overline{E}_t = D_3 \left\{ \frac{1}{\mu_r} \overline{\overline{\alpha}}_1 \cdot \nabla_t \psi_1 \right\} - \widehat{u}_3 \times \nabla_t \psi_2 \tag{11a}$$

$$\overline{\overline{L}}_h \cdot \overline{H}_t = D_3 \left\{ \frac{1}{\epsilon_r} \overline{\overline{\alpha}}_1 \cdot \nabla_t \psi_2 \right\} - \widehat{u}_3 \times \nabla_t \psi_1 \tag{11b}$$

In these equations we are employing vector-dyadic notation, where

$$\overline{E}_t = (h_1 E_1) \widehat{u}_1 + (h_2 E_2) \widehat{u}_2 \tag{12a}$$

$$\overline{H}_t = (h_1 H_1) \widehat{u}_2 + (h_2 H_2) \widehat{u}_2 \tag{12b}$$

are the scaled transverse field vectors, while

$$\nabla_t = \widehat{u}_1 D_1 + \widehat{u}_2 D_2 \tag{13}$$

is a "gradient" operator in transverse (to $\hat{u}_3$) coordinates (u_1, u_2). The linear dyadic operators appearing on the left-hand side of (11) are given by

$$\overline{\overline{L}}_e = D_3\left\{\frac{1}{\mu_r}\overline{\overline{\alpha}}_1\, D_3\right\} + \epsilon_r\,\overline{\overline{\alpha}}_2 \tag{14a}$$

$$\overline{\overline{L}}_h = D_3\left\{\frac{1}{\epsilon_r}\overline{\overline{\alpha}}_1\, D_3\right\} + \mu_r\,\overline{\overline{\alpha}}_2 \tag{14b}$$

where the $\overline{\overline{\alpha}}_i$-dyadics in (11) and (14) are defined as

$$\overline{\overline{\alpha}}_1(\overline{r}) = \alpha_2^{-1}(\overline{r})\hat{u}_1\,\hat{u}_1 + \alpha_1^{-1}(\overline{r})\hat{u}_2\,\hat{u}_2 \tag{15a}$$

$$\overline{\overline{\alpha}}_2(\overline{r}) = \alpha_1(\overline{r})\hat{u}_1\,\hat{u}_1 + \alpha_2(\overline{r})\hat{u}_2\,\hat{u}_2 \tag{15b}$$

In *local* spatial domains, where μ_r and ϵ_r are functions of (u_1, u_2), but not of u_3, (we will employ this approximation in the numerical work that follows) the second-order DE's in (11) simplify to

$$\overline{\overline{L}}\cdot\overline{E}_t = D_3\{\overline{\overline{\alpha}}_1\cdot\nabla_t\,\psi_1\} - \mu_r\,\hat{u}_3\times\nabla_t\,\psi_2 \tag{16a}$$

$$\overline{\overline{L}}\cdot\overline{H}_t = D_3\{\overline{\overline{\alpha}}_1\cdot\nabla_t\,\psi_2\} - \epsilon_r\,\hat{u}_3\times\nabla_t\,\psi_1 \tag{16b}$$

with the single dyadic operator given by

$$\overline{\overline{L}}(\overline{r}) = D_3\{\overline{\overline{\alpha}}_1\, D_3\} + \mu_r\,\epsilon_r\,\overline{\overline{\alpha}}_2 \tag{17}$$

Now that the transverse field generating equations have been developed, it may be worth comparing them to the classical formulation for TE and TM modes in straight waveguide sections. In particular, if we set $u_3 = z$ and assume homogeneous constitutive parameters, we can partially separate variables in (16), using an $\exp(-\gamma z)$ propagation factor. The result will be explicit functional relationships yielding the transverse (to z) fields $\overline{E}_t$ and $\overline{H}_t$ in terms of transverse derivatives of $\psi_1 = E_z$ and $\psi_2 = H_z$, where we note that the h_3 scale factor in (9) is unity. These are the standard waveguide field generating equations shown, for instance, by Silver in [16].

The CP formulation is thus an extension to these earlier waveguide field ideas, with *spatial curvature* being introduced here in the u_3

direction of propagation. This curvature prohibits (except for $\gamma = 0$) the separation of the fields into the usual TE and TM (to u_3) subfields, as is permitted when using a linear coordinate (e.g. $u_3 = z$). The TE and TM field partitioning results by the optional decoupling of the CP's, each of which is found to solve the usual Helmholtz operator eigenvalue problem in the transverse cross section of the waveguiding structure. For the general case of curvilinear coordinates, the CP's remain coupled, satisfying a more complex relationship, as we will now investigate.

c. *Coupled Potential Interactions*

The solution of either the first-order (6) or second-order (11) forms of the transverse field generating equations offers the means to evaluate E_1, E_2, H_1 and H_2 through an assumed knowledge of the potentials $\psi_1 = h_3 E_3$ and $\psi_2 = h_3 H_3$. To complete the analytical development of the CP formulation we need to consider the necessary equations from which to obtain the potentials. A direct approach is to utilize the remaining Maxwell's equations in (4) that were not used for transverse field generation. These two equations, namely (4c) and (4f), can be expressed as

$$\epsilon_r \alpha_3 \psi_1 - \widehat{u}_3 \cdot \nabla_t \times \overline{H}_t = 0 \tag{18a}$$

$$\mu_r \alpha_3 \psi_2 - \widehat{u}_3 \cdot \nabla_t \times \overline{E}_t = 0 \tag{18b}$$

The use of (18) for computing the CP's requires the explicit substitution of $\overline{E}_t$ and $\overline{H}_t$ obtained from solutions of either (6) or (11). At this stage in the development, we can express these solutions in the sense of *formal* inverses to $\overline{\overline{L}}_e$ and $\overline{\overline{L}}_h$. These dyadic operators, as defined in (14), can be "inverted" by approximate numerical methods. The simplifying idea is to consider the operators as ordinary DE's in the u_3-coordinate, with (u_1, u_2) held constant. An example of this type of process will be considered in section 6.3.

After numerically eliminating $\overline{E}_t$ and $\overline{H}_t$ from (18), there remains the problem of solving for the CP's. Enforcement of the DE's in (18) can be performed by the well-known method of weighted residuals [17] (known as the moment method when applied to integral equations in electromagnetics). It is this approach that will be developed later in this chapter. The result will be a set of *Galerkin* equations for the potentials where the basis (expansion) and weighting (testing) functions will come from the same set.

An alternate procedure for the solution of the potentials is to employ a generalized variational principle for isotropic media, based upon self-reaction [18]. The interior region solution of Maxwell's equations, for specified Dirichlet boundary conditions of the CP's on an enclosing surface, S, will yield the stationary point of the following complex energy-power functional

$$F = \jmath k_0 \iiint\limits_V \epsilon_r \overline{E} \cdot \overline{E} - \mu_r \overline{H} \cdot \overline{H} \, dv - \iint\limits_S \overline{E} \times \overline{H} \cdot \widehat{n} \, dS \qquad (19)$$

To make this a functional solely of the potentials, one can substitute $\psi_1 = h_3 E_3$ and $\psi_2 = h_3 H_3$ and replace $\overline{E}_t$ and $\overline{H}_t$ by their formal inverse relationships to the CP's. As for the case of the Galerkin approach, the transverse fields are obtained numerically in terms of discrete spatial point values of the potentials. We will consider, by example, how this is done in section 6.3.

Before proceeding, it is worthwhile at this stage to summarize the key steps that have been described:

(1) Using generalized orthogonal coordinates, Maxwell's curl equations were rewritten to yield coupled first-order PDE's in (6) for the scaled transverse (to $\widehat{u}_3$) field components in terms of the transverse derivatives of the scaled longitudinal field components, which are defined to be the coupled potentials: $\psi_1 = h_3 E_3$ and $\psi_2 = h_3 H_3$. These "state-equations" are implicitly of second-order in u_3.

(2) By cross-substituting between these equations, the second-order set of PDE's is found (11) for generating the transverse field components in terms of the derivatives of the CP's.

(3) The goal of the derivation is to recast the vector field problem in the inhomogeneous media into one of dealing only with the two scalar CP's. Through employing a numerical inverse to either the first- or second-order generating equations, the desired reduction to a solution for the CP's can be attained. One way is to substitute the transverse field solutions into the remaining Maxwell's equations in (18). The other is to use the complex energy-power

functional in (19). Our numerical example in section 6.3 will illustrate this final elimination step via (18).

d. Circular Cylindrical Case

At this juncture we will take a brief diversion to reexpress the CP formulation in circular cylindrical coordinates. This will serve as an example of applying the generic curvilinear expressions to a commonly used coordinate system. In addition, these specialized expressions will be employed in the computational validations that will be considered in the next two sections.

Using circular cylindrical coordinates $(u_1, u_2, u_3) = (z, \rho, \phi)$, the scale factors are given by $h_1 = h_2 = 1$ and $h_3 = \rho$. Note that we have not followed the standard (ρ, ϕ, z) ordering. The reason for this is to identify the ϕ coordinate as u_3, which is assumed to be periodic, while retaining a "right-hand" system. Continuing, the wavenumber multiplied scale factor ratios in (5) become $\alpha_1 = \alpha_2 = k_0\,\rho$ while $\alpha_3 = k_0/\rho$.

Noting that $D_1 = D_z$, $D_2 = D_\rho$, while $D_3 = D_\phi$, the dual first-order systems in (6) can be combined into a single equation

$$D_\phi \overline{\overline{V}}(\overline{r}) + \overline{\overline{M}}(\overline{r}) \cdot \overline{\overline{V}}(\overline{r}) = \overline{\overline{U}}(\overline{r}) \tag{20}$$

Since $\overline{\overline{M}}_1 = \overline{\overline{M}}_2$, only one cross-coupling array,

$$\overline{\overline{M}}(\overline{r}) = k_0\,\rho \begin{bmatrix} 0 & \mu_r(\overline{r}) \\ -\epsilon_r(\overline{r}) & 0 \end{bmatrix} \tag{21}$$

needs to be used for the case of circular cylindrical coordinates. In addition, the $\overline{V}_p$ vectors in (8) and the $\overline{U}_p$ vectors in (10) have each been respectively combined to form the columns of individual 2 × 2 arrays,

$$\overline{\overline{V}}(\overline{r}) = \begin{bmatrix} E_z & E_\rho \\ -H_\rho & H_z \end{bmatrix} \tag{22}$$

and

$$\overline{\overline{U}}(\overline{r}) = \begin{bmatrix} D_z \psi_1 & D_\rho \psi_1 \\ -D_\rho \psi_2 & D_z \psi_2 \end{bmatrix} \tag{23}$$

The CP's in (23) are found from (9), via $\psi_1 = \rho E_\phi$ and $\psi_2 = \rho H_\phi$.

Since $\alpha_1 = \alpha_2$ in (15), the two dyad components of $\overline{\overline{\alpha}}_1$ are equal, as are the two components of $\overline{\overline{\alpha}}_2$. The second-order PDE systems in (14) can thus be simplified, resulting in non-dyadic forms

$$\mathcal{L}_e \overline{E}_t = D_\phi \{\frac{1}{\mu_r} \nabla_t \psi_1\} - k_0 \rho \widehat{\phi} \times \nabla_t \psi_2 \tag{24a}$$

$$\mathcal{L}_h \overline{H}_t = D_\phi \{\frac{1}{\epsilon_r} \nabla_t \psi_2\} - k_0 \rho \widehat{\phi} \times \nabla_t \psi_1 \tag{24b}$$

In these equations, the transverse fields (with $h_1 = h_2 = 1$) are

$$\overline{E}_t = E_\rho \widehat{\rho} + E_z \widehat{z} \tag{25a}$$

$$\overline{H}_t = H_\rho \widehat{\rho} + H_z \widehat{z} \tag{25b}$$

while

$$\nabla_t = \widehat{\rho} D_\rho + \widehat{z} D_z \tag{26}$$

is the transverse (to $\widehat{\phi}$) gradient operator. The linear operators appearing on the left-hand side of (24) are given by

$$\mathcal{L}_e = D_\phi \{\frac{1}{\mu_r} D_\phi\} + \epsilon_r (k_0 \rho)^2 \tag{27a}$$

$$\mathcal{L}_h = D_\phi \{\frac{1}{\epsilon_r} D_\phi\} + \mu_r (k_0 \rho)^2 \tag{27b}$$

e. *Axisymmetric Specialization*

Before proceeding to the numerical implementation of the CP formulation, let us briefly consider the special case of rotationally symmetric material. This will illustrate the connection to the original coupled azimuthal potential (CAP) equations, as developed in [2–4] and Chapter 2. The CAP equations result as a special case of the CP formulation.

For the case of local spatial domains where μ_r and ϵ_r are functions of $(u_1, u_2) = (z, \rho)$, but not of $u_3 = \phi$, as considered in deriving (16) and (17), the PDE's in (24) simplify to

$$\mathcal{L}\,\overline{E}_t = D_\phi \nabla_t \psi_1 - \mu_r k_0 \rho \hat{\phi} \times \nabla_t \psi_2 \tag{28a}$$

$$\mathcal{L}\,\overline{H}_t = D_\phi \nabla_t \psi_2 - \epsilon_r k_0 \rho \hat{\phi} \times \nabla_t \psi_1 \tag{28b}$$

where

$$\mathcal{L} = D_\phi^2 + \mu_r \epsilon_r (k_0 \rho)^2 \tag{29}$$

We now expand the field vectors in a Fourier series in the ϕ-coordinate

$$\overline{E}(\overline{r}) = \overline{E}_t(\overline{r}) + E_\phi(\overline{r})\hat{\phi} = \sum_{m=-\infty}^{\infty} \overline{e}_m(\rho, z) \exp(\jmath m\phi) \tag{30a}$$

$$\overline{H}(\overline{r}) = \overline{H}_t(\overline{r}) + H_\phi(\overline{r})\hat{\phi} = \sum_{m=-\infty}^{\infty} \overline{h}_m(\rho, z) \exp(\jmath m\phi) \tag{30b}$$

When these expansions are substituted into (28), it is found that the operation of $\mathcal{L}$ on the m-th modal transverse field reduces to a multiplication by

$$f_m(\rho, z) = \mu_r(\rho, z)\, \epsilon_r(\rho, z)\, (k_0 \rho)^2 - m^2 \tag{31}$$

The modal transverse field vectors are then obtained by using

$$\overline{e}_{t,m}(\rho, z) = f_m^{-1} [\jmath m \nabla_t \psi_{1,m} - \mu_r k_0 \rho \hat{\phi} \times \nabla_t \psi_{2,m}] \tag{32a}$$

$$\overline{h}_{t,m}(\rho, z) = f_m^{-1} [\jmath m \nabla_t \psi_{2,m} - \epsilon_r k_0 \rho \hat{\phi} \times \nabla_t \psi_{1,m}] \tag{32b}$$

where the m-th order modes of the CAP's are

$$\psi_{1,m}(\rho,z) = \rho\, e_{\phi,m}(\rho,z) \tag{32c}$$

$$\psi_{2,m}(\rho,z) = \rho\, h_{\phi,m}(\rho,z) \tag{32d}$$

as was found in the original axisymmetric CAP formulation [2–4].

Thus, by employing a Fourier series field expansion within axisymmetric material, we can obtain an exact analytical inverse to the transverse field generating equations on a mode-by-mode basis. A pathological case exists, however. When dealing with lossless material, where μ_r and ϵ_r are both *real* spatial functions, the $f_m(\rho,z)$ denominator in the transverse field equations above will be zero on spatial surfaces where

$$k_0\, \rho = \frac{|m|}{\sqrt{\mu_r(\rho,z)\, \epsilon_r(\rho,z)}} \tag{33}$$

On these surfaces, the generating equations in (32) become indeterminate and the operator in (29) will have complementary (undriven) solutions which satisfy the requisite periodicity. These resonant solutions are similar in nature to modes in microstrip ring-resonators or quantum states of atoms. A practical concern, to be considered in section 6.4, is that numerical difficulties may arise close to these radii.

If the Fourier series in (30) are used in the general inhomogeneous case, as is embodied in (24), the individual m-th order modes will not decouple from one another. Furthermore, if either μ_r or ϵ_r have azimuthal discontinuities then the resultant ϕ-coordinate step functions in the respective H_ϕ or E_ϕ will produce pointwise convergence difficulties in the Fourier series, *a la* the Gibbs phenomenon [19].

For the case of material that has a slowly varying inhomogeneity in ϕ, a possible approach is to employ the Fourier expansions in (30), as well as azimuthal Fourier series for both μ_r and ϵ_r. This concept is considered by Fleming in Chapter 2 of this text and in [11]. The resultant convolutions of the field modes and the material modes can be truncated to provide approximate generating equations for the transverse fields in the form of algebraic linear systems. By assuming a quasi-axisymmetric case, where only a few terms are needed in the Fourier series for the media, this approach may be a viable alternative to that which is considered here.

The CAP formulation is completed by developing the equations from which to obtain the potentials, ψ_1 and ψ_2. One approach is to substitute the transverse field expressions in (32) into the two Maxwell's equations in (18), rewritten in circular cylindrical coordinates as

$$k_0\,\epsilon_r\,E_\phi - \widehat{\phi}\cdot\nabla_t\times\overline{H}_t = 0 \tag{34a}$$

$$k_0\,\mu_r\,H_\phi - \widehat{\phi}\cdot\nabla_t\times\overline{E}_t = 0 \tag{34b}$$

The substitution of $\overline{E}_t$ and $\overline{H}_t$, as found from (32), into (34) will yield a pair of 2nd-order coupled PDE's for the modal potentials. This was the procedure that was used in deriving the original CAP equations. The coupled PDE's for $\psi_{1,m}$ and $\psi_{2,m}$ appear in equations (5a) and (5b) of Chapter 2.

The complex functional in (19) was mentioned as an alternative to the weighted residual enforcement of (18). This type of variational approach was used in developing most of the finite element algorithms for scattering involving rotationally symmetric objects. The complex functional for the CAP's was found by using either of two equivalent general principles relating differential and variational formulations: the *Euler-Lagrange* equations [20] and the *stationary* theorem [21]. These approaches lead to a functional which is similar to the general form in (19) for this special case. The details of the derivation are in [3] while the results are discussed by Fleming in section 2.3.

6.3 Numerical Algorithm

a. *Finite Element Mesh*

We will employ a finite element method (FEM) using the special $u_3 = \phi$ form of circular cylindrical coordinates, as was considered in subsection 6.2d: namely, (z, ρ, ϕ). The building block for the FEM in static and time-harmonic problems is the spatial element, of which there are numerous standard forms [17]. In this case, we will span the desired region of 3-D space using multi-element rings and disks, as is depicted in Fig. 2. Disks are rings of elements having zero inner radius; they are connected to the z-axis. The rings are each composed of N pentahedral elements while the disks are constructed from N quadrahedral elements.

Within each element, the basis functions for E_ϕ and H_ϕ will have quadratic variation in the transverse (z, ρ) coordinates while being con-

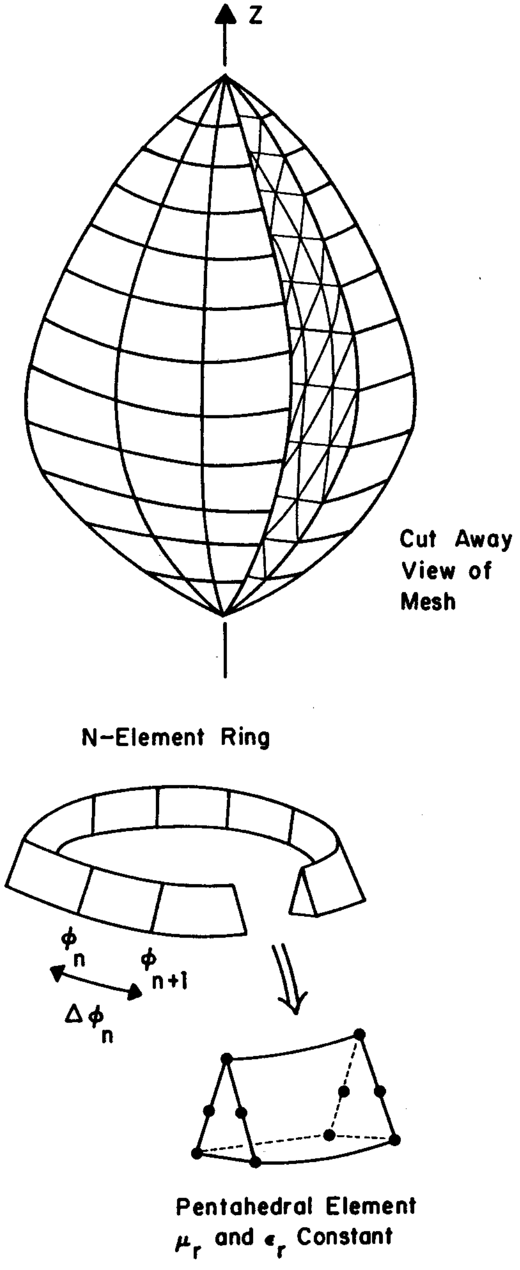

Figure 2 Finite element mesh and *N*-element ring.

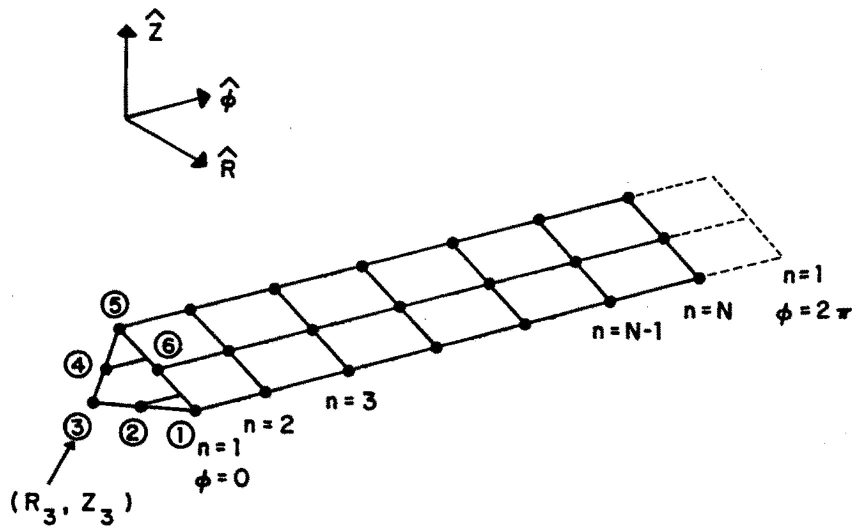

Figure 3 Nodal topology of unwrapped N-element ring.

stant in ϕ. The transverse fields, $\overline{E}_t$ and $\overline{H}_t$, will also have a quadratic approximation in the transverse coordinates, while having *natural* basis function ϕ-variations which conform analytically to the assumed basis function behavior of ψ_1 and ψ_2.

Within each element, the generally complex-valued material parameters, ϵ_r and μ_r, are assumed to be spatially constant. These elements will, by necessity, have dimensions which are much smaller than the wavelength. At the same time, the elements will be small enough to accurately resolve the spatial material variation of the structure being modeled.

b. Discrete Transport Equation

Let us now consider the numerical solution, within each ring or disk, for the transverse fields in terms of ψ_1 and ψ_2. Referring to Fig. 3, which is an opened out version on one of the element "rings" in Fig. 2, we will seek a discrete form of (20) that relates the transverse field arrays at the triangular end-segments (in ϕ) of the n-th element. Such a transport equation will take the form

$$\overline{\overline{V}}_{n+1} = \overline{\overline{A}}_n \cdot \overline{\overline{V}}_n + \overline{\overline{B}}_n \tag{35}$$

where $\overline{\overline{V}}_n$ is a shorthand notation for $\overline{\overline{V}}(z, \rho, \phi_n)$. The subscript is used here to denote the array values at the n-th ϕ-step and should not be confused with the p-subscript used in (6) to indicate two types of $\overline{V}$-vectors. Respective transition and driving matrices, $\overline{\overline{A}}_n$ and $\overline{\overline{B}}_n$, will depend in part upon the ϕ-coordinate variations of the basis functions which are selected for the individual field components within the element.

A straightforward approach to discretizing (20) is to use central differences. This is based upon an assumed piecewise linear interpolate to the ϕ-variation of the various field components. To provide acceptable accuracy, this method was found to require very fine segmentation in ϕ, thus increasing the number of discrete unknowns in the solution.

c. *Natural Basis Functions*

A dramatic reduction in the required ϕ-resolution results from the use of "natural" basis functions for $\overline{\overline{V}}$ within each element. These bases are exact analytical solutions within the element for the assumed functional form of ψ_1 and ψ_2. The initial approach used to obtain the natural basis functions was to solve the first-order system in (20), using the variation of parameters method [22]. This first required finding the complementary solutions of (20), when $\overline{\overline{U}} = \overline{\overline{0}}$, and is lengthy to describe. A more concise technique, which yields the same result, solves the second-order system in (28). As an example, by defining the driving vector on the right-hand side of (28a) as

$$\overline{P} = D_\phi \nabla_t \psi_1 - \mu_r k_0 \rho \hat{\phi} \times \nabla_t \psi_2 \tag{36}$$

and noting that μ_r and ϵ_r are assumed constant *in the element*, we obtain the general solution [22]

$$\begin{aligned} \overline{E}_t(z, \rho, \phi) = & C_1(z, \rho) \sin(\beta\phi) + C_2(z, \rho) \cos(\beta\phi) \\ & + \beta^{-1} \int_0^\phi \overline{P}(z, \rho, \phi') \sin \beta(\phi - \phi')\, d\phi' \end{aligned} \tag{37}$$

with

$$\beta = k_0 \rho \sqrt{\epsilon_r \mu_r} \tag{38}$$

The vector functions $\overline{C}_1$ and $\overline{C}_2$ will depend upon the functional form of $\overline{P}$, as well as the boundary conditions on $\overline{E}_t$ at both ϕ_n and ϕ_{n+1}. A solution of (28b), for $\overline{H}_t$, will have a form that is similar to (37), but with different $\overline{C}$'s and a modified integrand, replacing $\overline{P}$.

We will employ pulse basis functions in the ϕ-coordinate for ψ_1 and ψ_2, thus giving a piecewise constant "staircase" interpolation around each multi-element ring or disk. This eliminates the D_ϕ-term in (36), giving a ϕ-constant $\overline{P}$-vector within the element,

$$\overline{P}(z,\rho) = -\mu_r\, k_0\, \rho\, \widehat{\phi} \times \nabla_t\, \psi_2 \tag{39}$$

A simplified form for (37) results, with the lower limit of the evaluated integration being added to the $\overline{C}_2$ term,

$$\overline{E}_t = \overline{C}_1(z,\rho)\,\sin(\beta\phi) + \overline{C}_2(z,\rho)\,\cos(\beta\phi) - \beta^{-2}\,\overline{P}(z,\rho) \tag{40a}$$

A similar result is obtained for the transverse magnetic field

$$\overline{H}_t = \overline{C}_3(z,\rho)\,\sin(\beta\phi) + \overline{C}_4(z,\rho)\,\cos(\beta\phi) - \beta^{-2}\,\overline{Q}(z,\rho) \tag{40b}$$

where

$$\overline{Q}(z,\rho) = -\epsilon_r\, k_0\, \rho\, \widehat{\phi} \times \nabla_t\, \psi_1 \tag{41}$$

The $\overline{C}_p$'s in (40) are *not* independent since the transverse fields in (28) must also satisfy (20). Upon substituting the vector components from (40) into (20), followed by some judicious algebraic manipulation to eliminate the vector function, $\overline{C}_p$'s within the element, the matrix components of the transport equation in (35) can be obtained

$$\overline{\overline{A}}_n = \begin{bmatrix} \cos(\beta\Delta\phi_n) & -\sqrt{\frac{\mu_r}{\epsilon_r}}\,\sin(\beta\Delta\phi_n) \\ \sqrt{\frac{\mu_r}{\epsilon_r}}\,\sin(\beta\Delta\phi_n) & \cos(\beta\Delta\phi_n) \end{bmatrix} \tag{42}$$

$$\overline{\overline{B}}_n = \begin{bmatrix} \beta^{-1}\,\sin(\beta\Delta\phi_n) & -\frac{1}{k_0\rho\epsilon_r}\{1-\cos(\beta\Delta\phi_n)\} \\ \frac{1}{k_0\rho\mu_r}\{1-\cos(\beta\Delta\phi_n)\} & \beta^{-1}\,\sin(\beta\Delta\phi_n) \end{bmatrix} \cdot \overline{\overline{U}}_n \tag{43}$$

where $\overline{\overline{U}}_n$, as defined by (23), does not vary with ϕ within the n-th element and $\Delta\phi_n = \phi_{n+1} - \phi_n$.

The numerical solution of the transport equation in (35) proceeds by defining a Riccati transform relationship [7]

$$\overline{\overline{V}}_{n+1} = \overline{\overline{R}}_n \cdot \overline{\overline{V}}_1 + \overline{\overline{S}}_n \tag{44}$$

Substitution into (35) gives the recurrence formulas

$$\overline{\overline{R}}_n = \overline{\overline{A}}_n \cdot \overline{\overline{R}}_{n-1} \tag{45}$$

$$\overline{\overline{S}}_n = \overline{\overline{A}}_n \cdot \overline{\overline{S}}_{n-1} + \overline{\overline{B}}_n \tag{46}$$

with initial conditions $\overline{\overline{R}}_1 = \overline{\overline{A}}_1$ and $\overline{\overline{S}}_1 = \overline{\overline{B}}_1$. These formulas are used to generate and store the $\overline{\overline{R}}_n$'s and $\overline{\overline{S}}_n$'s for n=1 to N, where N is the number of ϕ-segments. Enforcing the periodicity of the solution, using $\overline{\overline{V}}_{N+1} = \overline{\overline{V}}_1$, gives the initial condition to be used in (25)

$$\overline{\overline{V}}_1 = [\overline{\overline{I}} - \overline{\overline{R}}_N]^{-1} \cdot \overline{\overline{S}}_N \tag{47}$$

where $\overline{\overline{I}}$ is the 2×2 identity matrix.

d. Galerkin Method

Let us now consider additional details of the particular numerical approach that has been developed. Referring to the unwrapped element ring in Fig. 3, the potentials are represented within a multielement ring or disk by basis function expansions having the form

$$\psi_1(z,\rho,\phi) = k_0\,\rho \sum_{m=1}^{N} \sum_{k=1}^{6} e_\phi(m,k) 32\, q_k(z,\rho)\, p_m(\phi) \tag{48a}$$

$$\psi_2(z,\rho,\phi) = k_0\,\rho \sum_{m=1}^{N} \sum_{k=1}^{6} h_\phi(m,k)\, q_k(z,\rho)\, p_m(\phi) \tag{48b}$$

where the pulse functions are given by

$$p_m(\phi) = \begin{cases} 1 & \phi_m < \phi < \phi_{m+1} \\ 0 & \text{otherwise} \end{cases} \tag{49}$$

The quadratic basis function, q_k, has unit value at the k-th node within the triangular cross section of the element ring or disk, while being zero at each of the other 5 nodes. Explicit formulae are available for the q_k's [17]. The unknowns in (48) are the discrete field values, $e_\phi(m,k)$ and $h_\phi(m,k)$, which are defined, respectively, as E_ϕ and H_ϕ at the centers of the azimuthal arc-segments $(z,\rho) = (z_k,\rho_k)$, connecting each of the k-th nodes in the m-th element, again referring to Fig. 3.

The next step is to relate the transverse fields, using the natural basis functions, to the arc-segment values of E_ϕ and H_ϕ in (48). This is done by defining a numerical Green's dyadic, $\overline{\overline{G}}$, for the transverse field solution of the first-order transport equation in (20). The domain of the solution is the circular ϕ-contour composed of the j-th arc-segments within the multi-element ring or disk. The Green's dyadic that we seek will solve (20) with a diagonal $\overline{\overline{U}} = p_m(\phi)\overline{\overline{I}}$. More specifically,

$$D_\phi \overline{\overline{G}}(j,m,\phi) + \overline{\overline{M}}(z_j,\rho_j,\phi)\cdot\overline{\overline{G}}(j,m,\phi) = \begin{bmatrix} p_m(\phi) & 0 \\ 0 & p_m(\phi) \end{bmatrix} \tag{50}$$

The numerical solution to (50) is found by using the method embodied in (42) to (47), where the $\overline{\overline{U}}_n$ to be employed in (43) is the driving array defined above. Comparing (50) to (20), and using superposition in conjunction with (28), the transverse field array can be numerically evaluated along the (z_j,ρ_j) circular ϕ-contour by using

$$\overline{\overline{V}}(z_j,\rho_j,\phi) = \sum_{m=1}^{N}\sum_{k=1}^{6}\overline{\overline{G}}(j,m,\phi)\cdot\begin{bmatrix} e_\phi(m,k) & 0 \\ 0 & h_\phi(m,k) \end{bmatrix}\cdot\overline{\overline{DQ}}(j,k) \tag{51}$$

The DQ-array is given by

$$\overline{\overline{DQ}}(j,k) = \begin{bmatrix} D_z\{\rho\, q_k(z,\rho)\} & D_\rho\{\rho\, q_k(z,\rho)\} \\ -D_\rho\{\rho\, q_k(z,\rho)\} & D_z\{\rho\, q_k(z,\rho)\} \end{bmatrix} \tag{52}$$

which is evaluated at $(z,\rho) = (z_j,\rho_j)$. The transverse field array can now be expanded in the element cross section by use of quadratic basis functions in (z,ρ), giving

$$\overline{\overline{V}}(z,\rho,\phi) = \sum_{j=1}^{6} \overline{\overline{V}}(z_j,\rho_j,\phi)\, q_j(z,\rho) \tag{53}$$

The Galerkin equations are formed by weighted residual enforcement of (34), using the quadratic-pulse functions which first appeared in (48), $q_i(z,\rho)\,p_n(\phi)$, as weights. For each pair of unknown $e_\phi(n,i)$ and $h_\phi(n,i)$, we obtain the two weighted residual equations

$$\iiint q_i(z,\rho)\,p_n(\phi)\{k_0\,\epsilon_r\,E_\phi + D_\rho H_z - D_z H_\rho\}\,d\rho\,dz\,d\phi = 0 \tag{54a}$$

$$\iiint q_i(z,\rho)\,p_n(\phi)\{k_0\,\mu_r\,H_\phi + D_\rho E_z - D_z E_\rho\}\,d\rho\,dz\,d\phi = 0 \tag{54b}$$

These 3-D integrations are over all elements which share the (z_i,ρ_i) arc-segment in the support interval $\phi_n < \phi < \phi_{n+1}$. By substituting field components from (53) into (54) and performing the indicated array multiplications, we obtain the discretized versions of (54)

$$\begin{aligned}
& k_0 \sum_{k=1}^{6} e_\phi(n,k)\,\epsilon_r(n)\,W_1(i,k) \\
& + \sum_{m=1}^{N}\sum_{k=1}^{6} e_\phi(m,k)\left\{\sum_{j=1}^{6} T_{21}(j,m,n)\,W_2(i,j,k)\right\} \qquad\qquad (55a) \\
& + \sum_{m=1}^{N}\sum_{k=1}^{6} h_\phi(m,k)\left\{\sum_{j=1}^{6} T_{22}(j,m,n)\,W_3(i,j,k)\right\} = 0
\end{aligned}$$

and

$$k_0 \sum_{k=1}^{6} h_\phi(n,k)\,\mu_r(n)\,W_1(i,k)$$

$$- \sum_{m=1}^{N} \sum_{k=1}^{6} h_\phi(m,k) \left\{ \sum_{j=1}^{6} T_{21}(j,m,n)\,W_2(i,j,k) \right\} \tag{55b}$$

$$+ \sum_{m=1}^{N} \sum_{k=1}^{6} e_\phi(m,k) \left\{ \sum_{j=1}^{6} T_{11}(j,m,n)\,W_3(i,j,k) \right\} = 0$$

where

$$T_{uv}(j,m,n) = \frac{1}{\Delta\phi_n} \int_{\phi_n}^{\phi_{n+1}} G_{uv}(j,m,\phi)\,d\phi \tag{56}$$

are the integrated elements of the Green's dyadic in (50), while

$$W_1(i,k) = \iint q_i(z,\rho)\,q_k(z,\rho)\,d\rho\,dz \tag{57a}$$

$$\begin{aligned} W_2(i,j,k) = {} & DQ_{12}(j,k) \iint q_i \cdot (D_\rho\, q_j)\,d\rho\,dz \\ & + DQ_{11}(j,k) \iint q_i \cdot (D_z\, q_j)\,d\rho\,dz \end{aligned} \tag{57b}$$

$$\begin{aligned} W_3(i,j,k) = {} & DQ_{22}(j,k) \iint q_i \cdot (D_\rho\, q_j)\,d\rho\,dz \\ & + DQ_{21}(j,k) \iint q_i \cdot (D_z\, q_j)\,d\rho\,dz \end{aligned} \tag{57c}$$

are products of elements of the DQ-array in (52) and moment integrals. These integrations can be evaluated analytically by using available formulae for polynomial integrands [17]. The relative complex material constants within the n-th element in the N-element ring or disk being considered are defined by $\epsilon_r(n)$ and $\mu_r(n)$. To complete the evaluation of the Galerkin equations in (54), one must add together the contributions of (55) from each ring or disk which is associated with the unknown $e_\phi(n,i)$ and $h_\phi(n,i)$. The result will be a sparse linear system, which can be made to have a banded block structure by proper ordering of the azimuthal field unknowns. Driving the sparse linear system will be the contributions from (55) which entail "known" boundary values of $e_\phi(m,k)$ and $h_\phi(m,k)$ at the exterior surface surrounding the finite element mesh.

6.4 Computer Validations

a. *Transverse Fields*

The numerical algorithm for generating the transverse fields from the potentials was extensively tested before being used to implement the Galerkin equations. One set of tests imposed azimuthal field boundary conditions, using an obliquely incident, TM-polarized, plane wave having magnitude $E^i = 10V/m$, at the $6N$ arc-segments of an isolated N-element ring or disk, as is illustrated in Fig. 4. Transverse fields were then computed at the $6N$ point-nodes and compared to the known field components for cases of lossy and lossless media. These are *not* scattering solutions since the boundary values are known. All computations described in this chapter were performed with single precision (32 bit) arithmetic using compiled FORTRAN 77 source code on an 80386 based personal computer using an 80387 math coprocessor.

Example calculations appear in Figs. 5 and 6, where the magnitudes and phases of E_ρ are compared to the exact field of a $\theta^i = 45°$ canted incidence plane wave at the point-nodes on the circular contour, (z_1, ρ_1, ϕ_n) for $n = 1$ to N. In the free space case of Fig. 5, the contour radius is $\rho = 1.0\lambda_0$, while the radius is $\lambda_0/2$ in the $\epsilon_r = 4 - \jmath 1$ case of Fig. 6. The right-angle sides in the triangular element cross section are $\lambda_0/15$ in length for the free-space case and are $\lambda_0/30$ in length for the lossy material case. Convergence data are summarized for the free space case in Table 1, which lists the RMS percentage errors of the computed transverse field components versus the number of ϕ-segments in the ring, N, and the size of the right-angle sides of the triangular elements. An obvious implication of this data is that

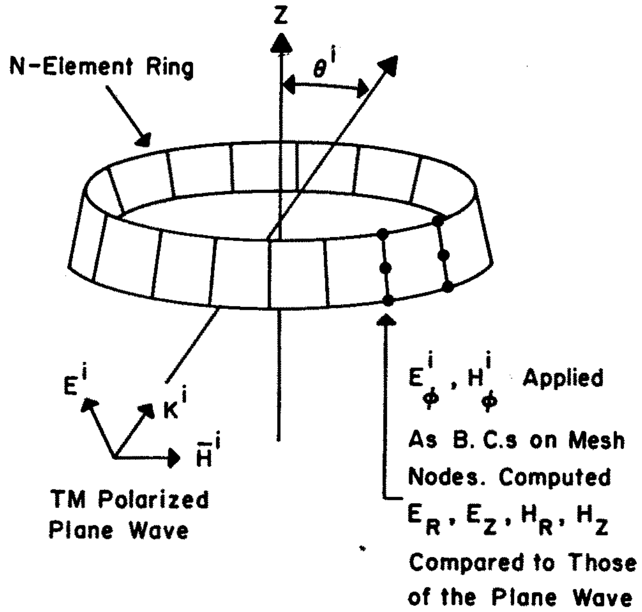

Figure 4 Element ring transverse field testing.

convergence to a lower error level requires both increases in N and reductions in the meridian element dimensions.

Table 1. Percentage Errors in Transverse Fields

	$L = \lambda_0/10$			$L = \lambda_0/15$			$L = \lambda_0/20$		
N	E_ρ	E_z	H_ρ	E_ρ	E_z	H_ρ	E_ρ	E_z	H_ρ
16	15	23	19	12	23	19	12	23	19
32	7	5	5	4	5	4	2	5	4
64	6	4	5	3	2	2	2	1	1

Computed fields are evaluated on an N-element ring of radius $1\lambda_0$ for a triangular element with right-angle sides of length L.

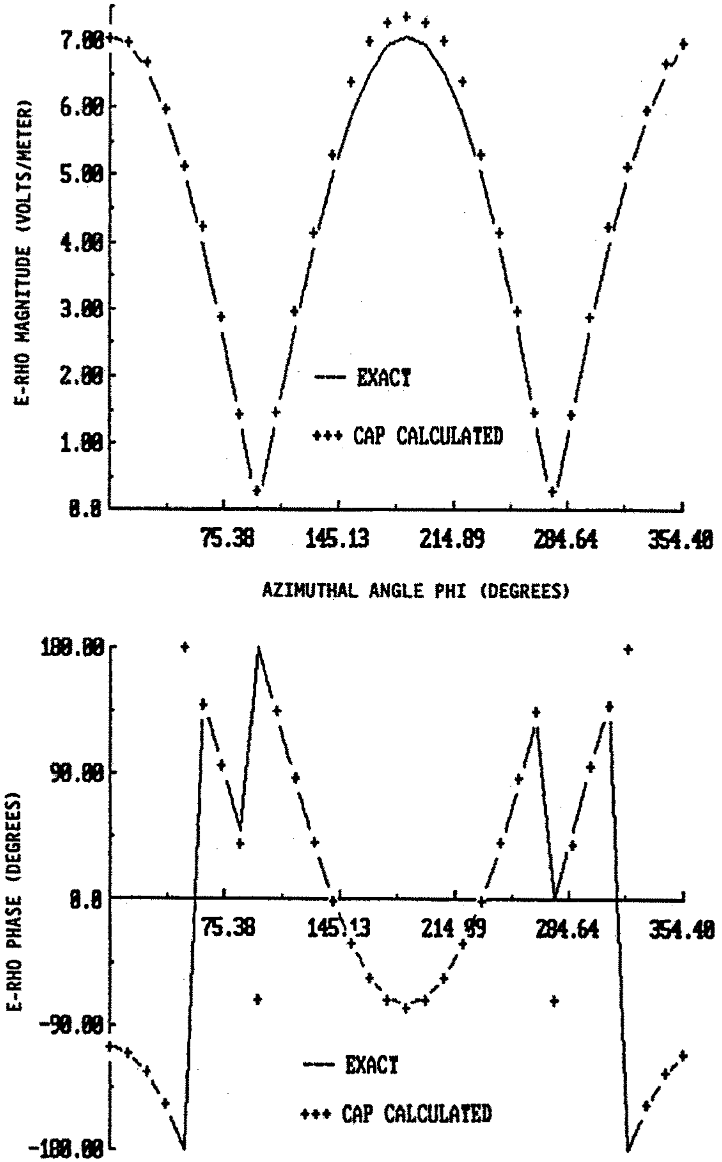

Figure 5 Comparison of CAP calculated and exact E_ρ at $\rho=1.0\lambda_0$ for plane wave in free space having $E^i=10$ V/m, with $L=\lambda_0/15$ and $N=32$. (a) Magnitude comparison. (b) Phase comparison.

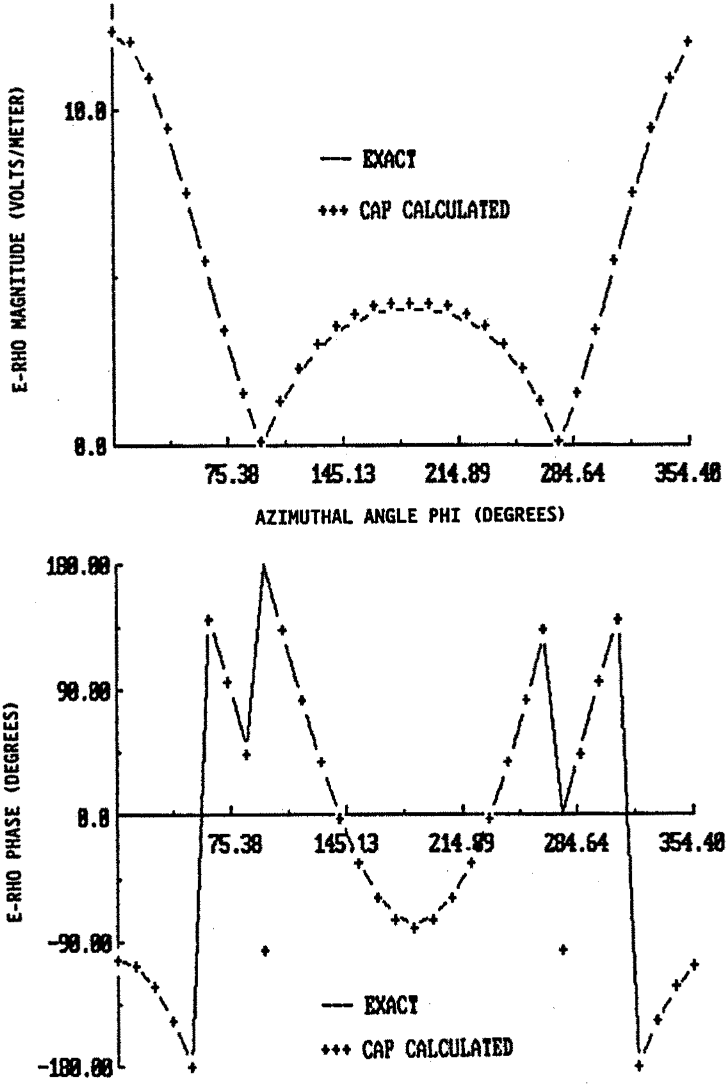

Figure 6 Comparison of CAP calculated and exact E_ρ at $\rho=\lambda_0/2$ for a plane wave in $\epsilon_r = 4 - j$ with $L=\lambda_0/30$ and $N=32$. (a) Magnitude comparison. (b) Phase comparison.

The convergence tests were repeated for a wide variety of radii, materials and element sizes. In addition, known field configurations involving spherical and cylindrical harmonics were used. These various tests established the need for quadratic elements in the q_k's of (48), vice linear elements which were first used. Also, the development of the natural basis functions was motivated by the slow convergence of early tests which used central differences in ϕ to discretize equation (20).

The effect of resonant solutions on the transverse field equations was also studied. As was noted in section 6.2, $\overline{E}_t$ and $\overline{H}_t$ (or $\overline{\overline{V}}$) can have non-zero periodic solutions over contours with radius defined in (33), *without* being driven by the CP's. These resonant solutions will thus tend to induce ill-conditioning of the numerical solution near these radii, in a similar manner to that observed for surface integral equations at frequencies near that of the cavity resonances of the enclosed volume. An important question that was initially addressed is: what is the spatial sensitivity about the resonant radius in the presence of low material losses? The transverse field generating program was used to test plane wave solutions for the N-element ring, as the radius of the $k = 1$ node contour was stepped through a neighborhood of the resonance. The pointwise percentage errors in computing E_ρ at an element node in the proximity of the smallest resonant radius is shown in Fig. 7 for the case of a $\theta^i = 45°$ incident TM plane wave. The E_z and H_ρ had similar error profiles. Extensive tests revealed that for the lossless case, significant errors were induced at the nodes that came closer than about $\lambda_0/20$ to the resonant radius for the case of triangular element right angle sides having a length of $\lambda_0/10$.

For smaller element sizes, yielding enhanced accuracy of the gradient approximations used to drive the system in (20), this proximity effect became less severe, with closer approaches being tolerated. On the other hand, as N was increased beyond that needed to reduce the arc-segment size to about $\lambda/8$, no further error reduction was noted. This is to be expected since the natural basis functions are exact solutions to (20) for the pulse basis expansions in ϕ of the potentials. However, the gradients that drive (20) are being applied to the quadratic expansions for the potentials in (z, ρ) at the nodes of the triangles. This is akin to a "backward difference" formula and is well known to require small segmentation to converge well. The effect of a close-by resonant radius is to enhance the effects of *any* errors in the driver of

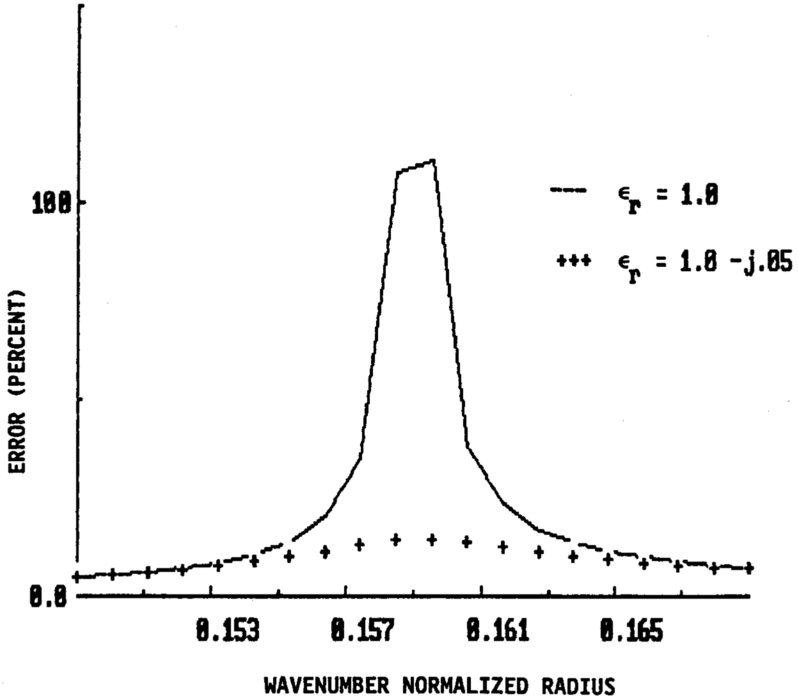

Figure 7 **Percentage error in E_ρ calculation at element node near $2\pi\rho=1$ resonant radius for lossless and low-loss cases. Element right-angle sides are $\lambda/15$.**

(20).

The resonance error problem was greatly alleviated by the introduction of even a slight loss in the material. This can be seen for the lossy case in Fig. 7, where the loss tangent is only 5%. Some possible numerical "fixes" for the resonant errors are to: (1) perturb the finite element mesh to put the singular radius at the midpoint between nodes; (2) introduce small losses in otherwise lossless material and; (3) seek out improved approximations for the potential gradients by employing better (z, ρ) basis expansions. Finally, it should be pointed out that the weighting integrals contained in the Galerkin equations in (54) tend to average these point-wise errors thus reducing the effects of the resonance instability.

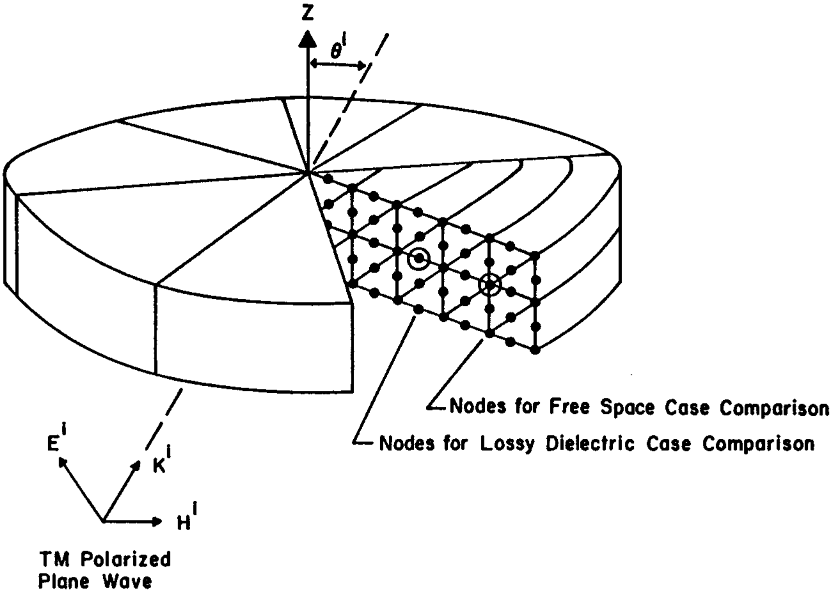

Figure 8 Cylindrical mesh used to test Galerkin solution for interior E_ρ and H_ϕ fields using plane wave boundary values on exterior surface.

b. Coupled Potentials

The discretized Galerkin equations in (55) were tested on a limited basis by computing the interior arc-segment values of E_ϕ and H_ϕ in the cylindrical finite element mesh which is displayed in Fig. 8. For the two examples to be considered, there were 8 azimuthal segments in the mesh, with 5 radial and 2 vertical increments, as is shown. This required the solution for a total of 480 complex unknowns which were generated by specified boundary values on the exterior surface of the cylinder. By forming vertical arrays, $\overline{X}_i$, composed of the 48 unknown E_ϕ and H_ϕ complex values in each of the 10 vertical mesh segments (3 nodes high and 8 segments around), the Galerkin equations produce a global linear system having the form

$$\begin{bmatrix} \overline{\overline{C}}_1 & \overline{\overline{D}}_1 & \overline{\overline{E}}_1 & & & & & \\ \overline{\overline{B}}_2 & \overline{\overline{C}}_2 & \overline{\overline{D}}_2 & & & & & \\ \overline{\overline{A}}_3 & \overline{\overline{B}}_3 & \overline{\overline{C}}_3 & \overline{\overline{D}}_3 & \overline{\overline{E}}_3 & & 0 & \\ & & \overline{\overline{B}}_4 & \overline{\overline{C}}_4 & \overline{\overline{D}}_4 & & & \\ & & & & \cdot & & & \\ & & 0 & & & \cdot & & \\ & & & & \overline{\overline{A}}_9 & \overline{\overline{B}}_9 & \overline{\overline{C}}_9 & \overline{\overline{D}}_9 \\ & & & & & & \overline{\overline{B}}_{10} & \overline{\overline{C}}_{10} \end{bmatrix} \begin{bmatrix} \overline{X}_1 \\ \overline{X}_2 \\ \overline{X}_3 \\ \overline{X}_4 \\ \cdot \\ \cdot \\ \overline{X}_9 \\ \overline{X}_{10} \end{bmatrix} = \begin{bmatrix} \overline{Y}_1 \\ \overline{Y}_2 \\ \overline{Y}_3 \\ \overline{Y}_4 \\ \cdot \\ \cdot \\ \overline{Y}_9 \\ \overline{Y}_{10} \end{bmatrix} \tag{58}$$

where the 48 × 48 complex sub-arrays, $\overline{\overline{A}}_i, \overline{\overline{B}}_i$, etc., are themselves sparse matrices. The $\overline{Y}_i$'s are formed from the boundary node contributions to (55).

There exist several methods for solving sparse blocked linear systems such as this [23]. A particularly simple approach was developed here, which implements the standard Gaussian elimination algorithm [24], but on a block-by-block basis. In such a scheme, the block submatrices and driving vectors are written to disk in sequence as they are generated. The system inversion is then performed by reading only the needed groups of these arrays into random access memory (RAM) at any one time. Such a procedure allows very large systems to be solved by using a minimum of RAM.

Magnitude and phase comparisons are shown for respective lossless and lossy cases in Figs. 9 and 10 for a $\theta^i = 45°$ TM-polarized incident plane wave. It should again be noted that this is not a scattering solution test: the incident field is applied only as a boundary condition for the potentials on the exterior surface. The Galerkin generated interior fields are then compared to the original plane wave along constant (z, ρ) circular contours inside of the mesh. The triangular element right-angle sides were $\lambda_0/15$ in the free space case and $\lambda_0/30$ in

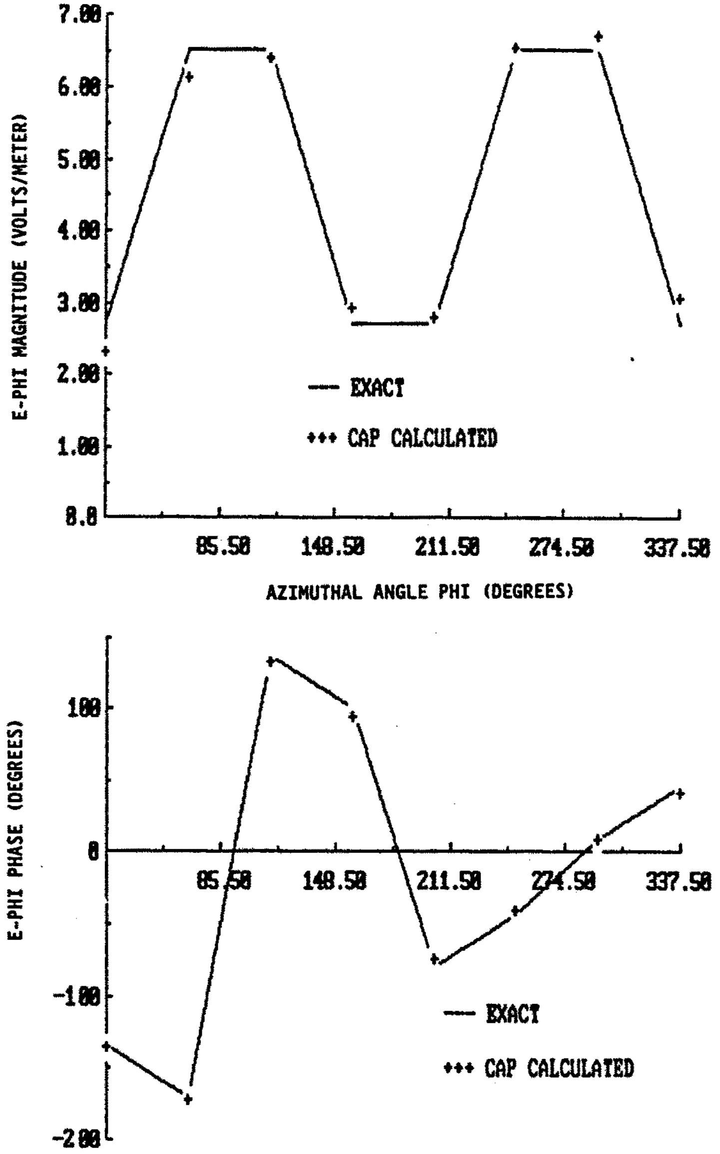

Figure 9 Comparison of CAP calculated and exact E_ϕ at $R=0.267\lambda_0$ for plane wave in free space with $L=\lambda_0/15$ and $N=8$. (a) Magnitude comparison. (b) Phase comparison.

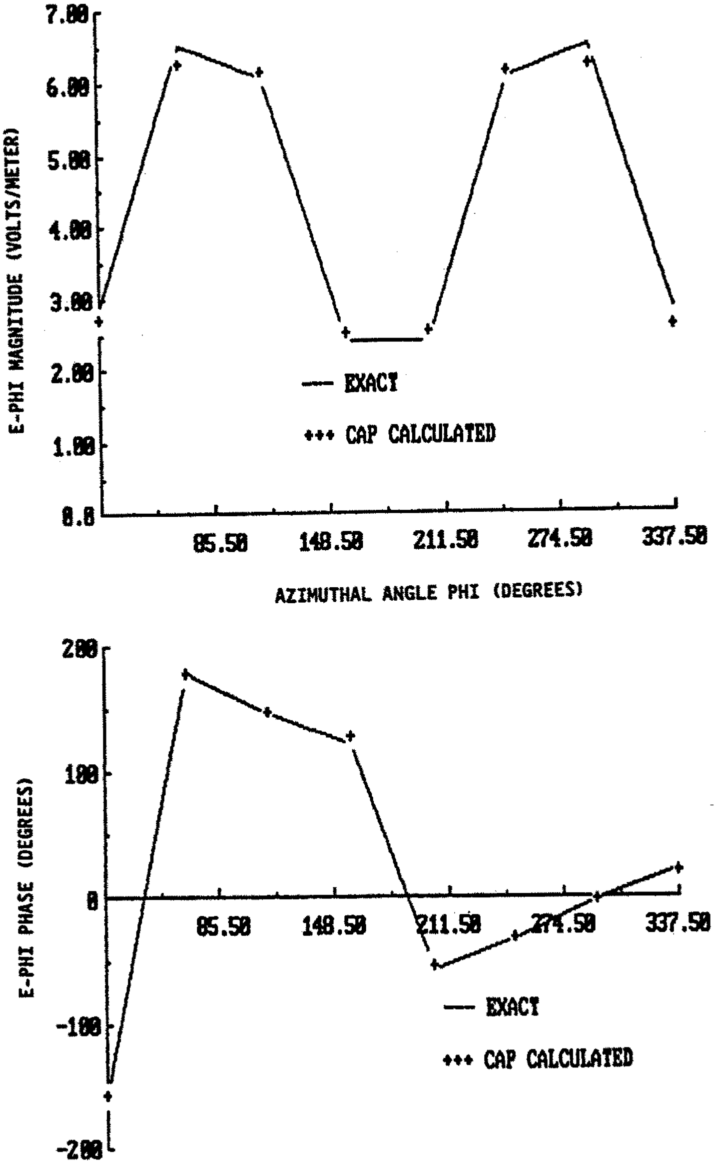

Figure 10 Comparison of CAP calculated and exact E_ϕ at $R=0.083\lambda_0$ for plane wave in $\epsilon_r=4$ - j with $L=\lambda/30$ and $N=8$. (a) Magnitude comparison. (b) Phase comparison.

the $\epsilon_r = 4 - \jmath 1$ case. In both instances, the outside circumference of the cylinder is over 2λ in the medium. The use of natural basis functions for the transverse fields yielded acceptable accuracy when using only $N = 8$ azimuthal segments over this outside circumference. Also, there are two resonant radii within the mesh for the lossless case. No increased errors in the Galerkin solution were observed for nodes that were close to these radii.

6.5 Discussion

The analytics and example numerics of a generalized coupled potential (CP) formulation have been described here along with the results of initial validations. These preliminary tests accompanied the development of basis functions for the potentials and the transverse field vectors. The sensitivity of the solutions to the instability of the generating equations near the singular radii in the lossless case was considered. This was followed by an example solution for the potentials within a cylindrical mesh subject to applied boundary values on the surface. A special block elimination method was used to solve the Galerkin equation sparse matrix system using a micro computer. Excellent accuracy was obtained in all such tests, having anywhere from a few hundred to well over a thousand complex unknowns. By employing faster Cray-class computers, this technique can readily handle hundreds of thousands of unknowns with computation times measured in minutes, not hours.

Future enhancements of the formulation are pending, in conjunction with numerous possible applications. For example, the use of circular rings will not be optimal for modeling some structures, such as aircraft, in that many extra elements may be required in the empty space surrounding the object. Circular rings were used in this initial implementation of the formulation, thus permitting convenient testing of its numerical performance for the special case of local circular cylindrical coordinates. By using more general orthogonal coordinate systems, as was initially considered in section 6.2, it should be possible to develop efficient numerical algorithms based on the CP formulation which can be applied to realistic 3-D material structures. Another option is to use non-circular rings and disks generated from elements having stepwise variable radii of curvature along each coordinate contour. In such a case, the sectionally curved elements become geometric building blocks for complex structures. The continuing development of this formulation will employ these and other enhancements to minimize the number of unknowns while increasing their solution accuracy.

The long-term goal is to employ this formulation for the computation of scattering by highly irregular and inhomogeneous material structures. This can be accomplished through the use of the *field feedback formulation* (F^3) [13], where the boundary value problem in the spatial region containing the scattering structure will be solved by using the coupled azimuthal potentials. This is conceptually related to the *boundary element method* (see Chapter 3) for coupling interior and exterior regions in a scattering problem. The boundary value solution will provide the "forward matrix operator" in the F^3. Used in conjunction with surface integrations to form the "feedback operator", the recursive linear system that results can be solved either directly or via iteration to obtain the scattered fields. A second possible option for scattering solution implementation is through a near field *radiation boundary condition*, examples of which are considered in Chapters 4, 5 and 8, as well as [14].

Acknowledgements

This research was sponsored by the Navy Direct Funding Program at the Naval Postgraduate School, Monterey, California.

References

[1] Bromwich, T. J. I'a., "Electromagnetic waves," *Phil. Mag.*, **S.6. 38**, No. 223, 143–164, 1919.

[2] Morgan, M. A., and K. K. Mei, "Numerical computation of E.M. scattering by inhomogeneous bodies of revolution," *Abstracts for the 1974 URSI Symposium on E.M. Wave Theory*, London, England, July, 1974.

[3] Morgan, M. A., S. K. Chang, and K. K. Mei, "Coupled potential formulation for 3-D E.M. boundary value problems in inhomogeneous axially symmetric media," *Abstracts for the 1975 IEEE/AP-S Symposium*, Urbana, IL, June 1975.

[4] Morgan, M. A., K. K. Mei, and S. K. Chang, "Coupled azimuthal

potentials for electromagnetic field problems in inhomogeneous axially-symmetric media," *IEEE Trans. Antennas Propagat.*, **AP-25**, 413–417, 1977.

[5] Stovall, R. E., and K. K. Mei, "Application of a unimoment technique to a biconical antenna with inhomogeneous dielectric loading," *IEEE Trans. Antennas Propagat.*, **AP-23**, 335–341, 1975.

[6] Mei, K. K., M. A. Morgan, and S. K. Chang, "Finite methods in electromagnetic scattering," Chap. 10 in *Electromagnetic Scattering*, P. L. E. Ushlenghi, Ed., New York: Academic Press, 1978.

[7] Morgan, M. A., and K. K. Mei, "Finite element computation of scattering by inhomogeneous penetrable bodies of revolution," *IEEE Trans. Antennas Propagat.*, **AP-27**, 202–214, 1979.

[8] Morgan, M. A., "Finite element computation of microwave scattering by raindrops," *Radio Science*, **15**, 1109–1119, 1980.

[9] Morgan, M. A., "Finite element calculation of microwave absorption by the cranial structure," *IEEE Trans. Biomed. Eng.*, **BME-28**, 687–695, 1981.

[10] Morgan, M. A., C. H. Chen, S. C. Hill, and P. W. Barber, "Finite element - boundary integral formulation for electromagnetic scattering," *J. Wave Motion*, **6**, 91–103, 1984.

[11] Fleming, A. H. J., *Numerical Analysis of Electromagnetic Scattering by Axisymmetric Composite Antenna Structures*, M.S. Thesis, Faculty of Technology, Chisholm, Inst. of Tech., Caulfield, Australia, March 1987.

[12] Mei, K. K., "Unimoment method of solving antenna and scattering problems," *IEEE Trans. Antennas Propagat.*, **AP-22**, 760–766, 1974.

[13] Morgan, M. A., and B. E. Welch, "The field feedback formulation for electromagnetic scattering problems," *IEEE Trans. Antennas Propagat.*, **AP-34**, 1377–1382, 1986.

[14] Kriegsmann, G. A., A. Taflove, and K. R. Umashankar, "A new formulation of electromagnetic wave scattering using an on-surface radiation boundary condition," *IEEE Trans. Antennas Propagat.*, **AP-35**, 153–161, 1987.

[15] Stratton, J. A., *Electromagnetic Theory*, New York: McGraw-Hill, 1941, Chap. 2.

[16] Silver, S., "Microwave Transmission Lines," Chap. 7 in *Microwave Antenna Theory and Design*, S. Silver, Ed., New York: McGraw-Hill, M.I.T. Rad. Lab. Series Vol. 12, 1949; (Reprinted) New York: Dover, 1965 and; London: Peregrinus, 1984.

[17] Lapidus, L., and G. F. Pinder, *Numerical Solution of Partial Differential Equations in Science and Engineering*, New York: Wiley Interscience, 1982, Chaps. 2 and 3.

[18] Jeng, S. K., and C. H. Chen, "On variational electromagnetics: theory and application," *IEEE Trans. Antennas Propagat.*, **AP-32**, 902–907, 1985.

[19] Oppenheim, A. V., and R. W. Schafer, *Digital Signal Processing*, Englewood Cliffs: Prentice-Hall, 1975, 238–241.

[20] Morse, P. M., and H. Feshbach, *Methods of Theoretical Physics*, New York: McGraw-Hill, 1953, 275-280.

[21] Stakgold, I., *Green's Functions and Boundary Value Problems*, New York: Wiley Interscience, 1979, 520–557.

[22] Greenberg, M. D., *Foundations of Applied Mathematics*, Englewood Cliffs: Prentice-Hall, 1978, 417–421.

[23] Tewarson, R. P., *Sparse Matrices*, New York: Academic Press, 1973.

[24] Golub, G. H., and C. F. Van Loan, *Matrix Computations*, Baltimore: John Hopkins Univ. Press, 1984, Chap. 4.